

<https://doi.org/10.1038/s43247-024-01255-4>

# Antarctic-wide ice-shelf firn emulation reveals robust future firn air depletion signal for the Antarctic Peninsula

Check for updates

Devon Dunmire <sup>1</sup> ✉, Nander Wever <sup>1,2</sup>, Alison F. Banwell <sup>3</sup> & Jan T. M. Lenaerts <sup>1</sup>

Antarctic firn is critical for ice-shelf stability because it stores meltwater that would otherwise pond on the surface. Ponded meltwater increases the risk of hydrofracture and subsequent potential ice-shelf collapse. Here, we use output from a firn model to build a computationally simpler emulator that uses a random forest to predict ice-shelf effective firn air content, which considers impermeable ice layers that make deeper parts of the firn inaccessible to meltwater, based on climate conditions. We find that summer air temperature and precipitation are the most important climatic features for predicting firn air content. Based on the climatology from an ensemble of Earth System Models, we find that the Larsen C Ice Shelf is most at risk of firn air depletion during the 21st century, while the larger Ross and Ronne-Filchner ice shelves are unlikely to experience substantial firn air content change. This work demonstrates the utility of emulation for computationally efficient estimations of complicated ice sheet processes.

Between 1992 and 2020, Antarctic Ice Sheet (AIS) mass loss contributed to  $7.4 \pm 1.5$  mm of global mean sea-level rise<sup>1</sup>. This mass loss occurs primarily via changes in ice dynamics and enhanced ice discharge<sup>2</sup> onto floating ice shelves, which surround 75% of the continent<sup>3</sup> and regulate the ocean-ward flow of inland ice<sup>4,5</sup>. As ice shelves weaken and thin, their buttressing effect reduces, allowing inland ice to flow faster into the ocean and creating a positive feedback loop for global sea-level rise<sup>6,7</sup>.

Several important processes have been identified as key to future ice-shelf thinning, weakening, and retreat including calving<sup>8</sup>, ocean-warming-induced basal melt<sup>9–11</sup>, and atmospheric-warming-induced surface melting<sup>12–14</sup>, the latter of which is of primary concern for this work. Atmospheric warming may result in ponded surface meltwater, subsequently triggering hydrofracture, whereby the hydrostatic pressure of ponded meltwater propagates fractures through the entire ice shelf<sup>15,16</sup>. Hydrofracture has been implicated in the break-up of several Antarctic ice shelves, including the 2002 near-complete disintegration of Larsen B<sup>17–19</sup> and the 2008 partial break-up of Wilkins<sup>20</sup>. However, hydrofracture is challenging to directly observe and has not been directly included in Antarctic ice sheet models, thus remaining a major source of uncertainty for assessing future sea level rise contributions from the Antarctic ice sheet<sup>2,21</sup>.

Currently, most Antarctic meltwater (94%) is retained within the porous firn layer<sup>22,23</sup>. However, if meltwater repeatedly refreezes without

sufficient firn replenishment via snowfall, the firn air content (FAC) decreases, limiting its ability to retain future meltwater, a process known as firn air depletion. Firn air depletion is a known precursor to hydrofracture, and thus plays an important role in ice-shelf stability<sup>24</sup>. There are many processes and factors that have been demonstrated or hypothesized to contribute to ice-shelf instability and potential collapse, including sea ice loss<sup>25</sup>, ice-shelf-fragment capsizing<sup>26</sup>, ice-shelf geometry<sup>27</sup>, föhn wind events<sup>28</sup>, atmospheric rivers<sup>29</sup>, hydrofracture<sup>17,18</sup>, and firn air depletion<sup>24</sup>.

As AIS melt is expected to increase nonlinearly with rising surface air temperatures throughout the 21st century<sup>30–32</sup>, the process of firn air depletion will become increasingly relevant on Antarctic ice shelves. This study addresses critical uncertainties related to hydrofracture by examining future firn depletion across all Antarctic ice shelves, providing insight into regions at risk of firn air depletion and the consequent heightened susceptibility to hydrofracture in a warming climate. Our multi-step methodology utilizes output from a physics-based firn model (SNOWPACK), which was forced with meteorological output from an Earth System Model (ESM), to train a statistical emulator using machine learning methods (Random Forest). Our emulator enables large-scale spatiotemporal FAC predictions.

First, for capturing surface melt and the impact of meltwater percolation on firn structure, we use the physics-based firn model

<sup>1</sup>Department of Atmospheric and Oceanic Sciences, University of Colorado, Boulder, CO, USA. <sup>2</sup>WSL Institute for Snow and Avalanche Research SLF, Davos, Switzerland. <sup>3</sup>Cooperative Institute for Research in Environmental Sciences (CIRES), University of Colorado, Boulder, CO, USA.

✉ e-mail: [devon.dunmire@colorado.edu](mailto:devon.dunmire@colorado.edu)

SNOWPACK<sup>33,34</sup>, which has been widely used in the polar regions<sup>35–39</sup>. Studies that use an almost identical “polar” SNOWPACK setup<sup>35–39</sup> show that the model exhibits good agreement with observed FAC across various climate regimes in Greenland<sup>38</sup>, as well as near-surface density profiles in the cold and dry Antarctic interior<sup>35</sup>, and agree with satellite observations and regional climate models on melt extent and volume on Antarctic ice shelves<sup>39</sup>. At 168 different ice-shelf sites (Fig. 1a), we force SNOWPACK with historical and future meteorological output from the Community Earth System Model version 2 (CESM2)<sup>40</sup> (see Sections 5.1.1 and 5.1.2).

In a warming climate, we expect meltwater, and thus ice lenses formed from refrozen meltwater, to become increasingly prevalent. In reality, ice lenses impede vertical meltwater percolation, and reduce FAC that can effectively be used for meltwater retention<sup>24,41</sup>. In SNOWPACK, water percolation is calculated using the ‘bucket scheme’, which has been regularly

used in model setups that reproduce density variations and ice layers in firn on the Greenland Ice Sheet in accordance with observations<sup>38,42–44</sup>. Currently however, there is no satisfying simulation approach for the effect of ice layers on water percolation in firn models<sup>42</sup>, which prevents us from directly assessing the impact of ice lenses on FAC. In our approach, we consider the impact of ice lenses on the ability of surface meltwater to access deeper parts of the firn by computing an effective FAC ( $FAC_e$ ) from the SNOWPACK model output (see Section 5.1.3). By including a relationship between ice lens thickness and permeability,  $FAC_e$  describes the reduction in FAC that can effectively be used for meltwater retention when ice lenses are present. We base this ice lens thickness-permeability relationship (TP1) on field observations of meltwater percolation through ice lenses on the Greenland Ice Sheet<sup>45,46</sup>. To assess remaining uncertainties regarding how thick ice lenses and slabs can grow before they limit the downward percolation of

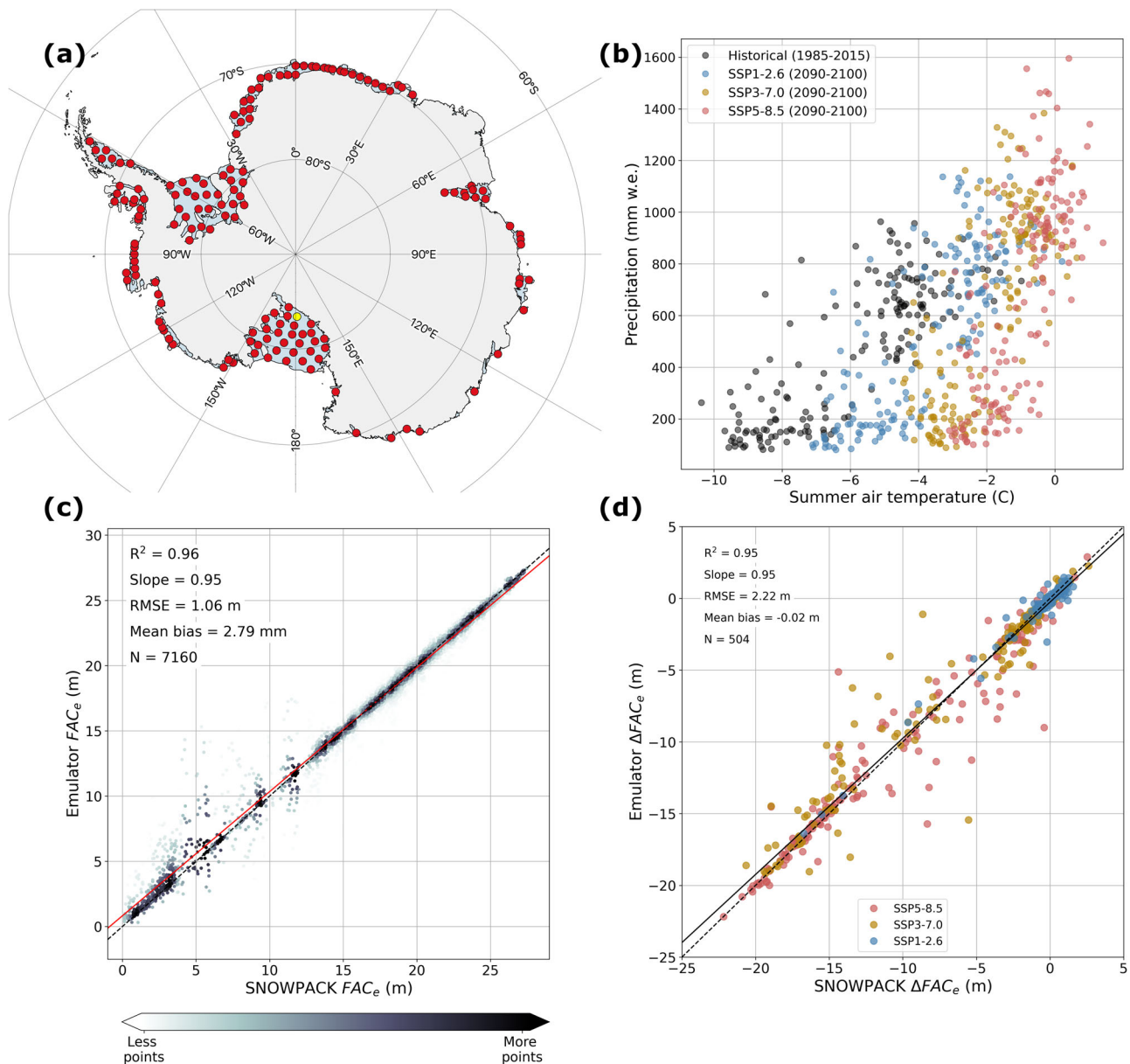


**Fig. 1 | Evaluation of emulator performance vs. SNOWPACK at ice-shelf sites.** **a** Map of 168 ice-shelf sites where the SNOWPACK model was forced with CESM2 historical and future output. The yellow dot represents the site featured in Fig. 2. **b** For each ice-shelf site, historical and future summer air temperature and annual precipitation, found by the emulator to be the most important parameters for determining future  $FAC_e$  **c** SNOWPACK-predicted  $FAC_e$  vs. emulator-predicted

$FAC_e$  for our independent testing dataset (includes data from both historical and future scenarios). Points are colored according to point density within 2 m  $FAC_e$  segments along the x-axis, beginning at 0 m. The red line represents the line of best fit. **d** 21st century  $\Delta FAC_e$  at each site from SNOWPACK and as predicted by our emulator, both forced with CESM2 climate output from the SSP1-2.6 (blue dots), SSP3-7.0 (golden dots), and SSP5-8.5 (red dots) future emission scenarios.

meltwater<sup>47</sup>, and the sensitivity this assumed relationship causes in the calculation of ice-shelf  $FAC_e$ , we define two alternative ice lens thickness-permeability relationships (TP2 and TP3), which are modified from TP1. Unless otherwise stated, we discuss results from the TP1 relationship.

Physical firn models such as SNOWPACK are computationally expensive to run, thus limiting our ability to comprehensively assess future firn conditions and associated uncertainties under a range of climate forcings. Therefore, we use the SNOWPACK-calculated  $FAC_e$  to build a firn emulator, i.e. a fast, statistically-driven approximation of a more sophisticated model<sup>48,49</sup> (see Section 5.2). We use a Random Forest regressor (RF) for our emulator because RFs have demonstrated good performance in emulating model processes<sup>50,51</sup>, can learn nonlinear behavior, and are quick to train and implement. Additionally, RFs provide out-of-bag estimates, a useful validation metric, and feature importance measures, allowing us to assess which climate conditions are most important for  $FAC_e$  predictions<sup>52</sup>.

Our emulator was trained to predict annual  $FAC_e$ , using 10-year moving means of current and future, widely available ice-shelf climate variables (mean annual and summer air temperature, total annual precipitation, and mean annual wind speed) from CESM2 model output (see Sections 5.2.1 and 5.2.2). We used 10-year moving means of these climate variables to effectively account for temporal dependencies related to firn memory and to largely remove interannual variability. After training our emulator, we first apply it to estimate historical (1985–2015) ice-shelf  $FAC_e$  from ERA5 global reanalysis output<sup>53</sup> (see Section 5.3.1). To predict 21<sup>st</sup> century change in  $FAC_e$  ( $\Delta FAC_e$ ), we run our emulator with changes in these climate variables from 35 different ESMs from the recent Coupled Model Intercomparison Project (CMIP6)<sup>54</sup> following 3 future (SSP) scenarios. The ESM-derived changes are added to the ‘current-state’ ERA5 climate (ERA5 +  $\Delta ESM$ , see Section 5.3.2). The emulated  $FAC_e$  predictions reveal long-term changes related to 21<sup>st</sup> century climate change. In this manuscript, we specifically focus on  $FAC_e$  changes over climatological time scales (as opposed to interannual  $FAC_e$  variability).

Recently, Veldhuijsen et al. (2023)<sup>55</sup> investigated future AIS  $FAC_e$  throughout the 21<sup>st</sup> century; however, they only use climatological forcing from CESM2, an ESM that has been demonstrated to have a relatively high climate sensitivity<sup>56</sup>. The authors highlight that future work should address this limitation by using an ensemble of ESMs. Here, our emulator allows for highly efficient ensembles of  $FAC_e$  predictions at large spatiotemporal scales using myriad readily available climate model output. We predict that by 2100, Larsen C Ice Shelf is most at risk of firn air depletion, while Ross and Ronne-Filchner, which buttress more upstream ice, are likely to experience little  $\Delta FAC_e$ . We further quantify uncertainties in our predictions of future ice-shelf firn air depletion and find that variability in ESM projections is the largest source of uncertainty, with the CMIP6-model range of  $\Delta FAC_e$  predictions for a given SSP greater than the spread between SSP scenarios.

## Results

### Emulator evaluation

After randomly selection 80% of our data for training, our emulator demonstrates good performance at predicting  $FAC_e$  on the remaining 20%. On this independent testing dataset, the emulator-predicted  $FAC_e$  explains 96% of the simulated SNOWPACK  $FAC_e$  variance, with a root mean squared error (RMSE) of 1.14 m and a mean bias of 14.8 mm (Fig. 1c). Our emulator also has an out-of-bag score of 0.955, indicating the high accuracy of the model performs on previously un-seen data samples. The emulator also generally does well at reproducing the total 21<sup>st</sup> century  $\Delta FAC_e$  (Fig. 1d) and follows the abrupt  $FAC_e$  changes observed in the SNOWPACK modeling (e.g. Fig. 2a). However, because the emulator is trained using 10-year moving averages of climate variables and SNOWPACK  $FAC_e$ , it does not simulate  $FAC_e$  changes as abruptly as SNOWPACK at a given site. Supplementary Fig. 1 shows that our emulator also reproduces total 21<sup>st</sup> century firn air depletion at an ice-shelf and regional scale as well, compared to that simulated by SNOWPACK (Emulator vs. SNOWPACK  $\Delta FAC_e$   $R^2 = 0.97$ ).

A key advantage of using a random forest is that it provides relative feature importance scores<sup>57</sup>, expressed by the so-called ‘Gini Index.’ The Gini Index scores sum to 1 across all input features and provide information about which features are most important for the model predictions<sup>52</sup>. For the input features used in this study, our emulator calculates the following Gini Index scores: 0.442 for mean summer air temperature, 0.327 for total annual precipitation, 0.122 for mean annual wind speed, and 0.109 for annual summer air temperature, indicating that summer air temperature and total precipitation are the most important climate features for predicting ice-shelf  $FAC_e$ . Summer air temperature influences  $FAC_e$  because it affects meltwater production in a strongly non-linear fashion<sup>39,58</sup>. Excessive surface meltwater refreezes in the firn to form ice lenses that impact vertical water percolation and severely deplete  $FAC_e$ <sup>24,41</sup>. With sufficient surface melt, thin ice layers can quickly merge to form thicker, impermeable ice slabs<sup>59–61</sup>, a process we observe in our SNOWPACK output forced with the CESM2 SSP5-8.5 scenario (Fig. 2). Counteracting the firn air depletion is firn replenishment via snowfall<sup>38,62</sup>, which constitutes the majority of the annual precipitation over Antarctic ice shelves, even in future warming scenarios<sup>63</sup>.

Substantial reductions in  $FAC_e$ , as depicted in Fig. 2a, are a direct outcome of the ice lens thickness-permeability relationship (TP1) we introduce to determine  $FAC_e$  as ice lenses develop, grow, and merge. For example, at the site shown in Fig. 2, we observe the formation of substantial ice lenses following the 2074 summer season (Fig. 2d), marked by higher-than-average summer air temperatures (Fig. 2a) and intensified melt. Despite relatively milder conditions during the 2075 melt season, these newly formed ice lenses inhibit the downward percolation of meltwater, which results in the formation of a larger ice slab (Fig. 2e) that continues to grow throughout the 21<sup>st</sup> century as meltwater repeatedly freezes on top of the ice slab (Fig. 2f). The abrupt  $FAC_e$  depletion event that occurs in 2075 is a consequence of our assumption that ice lenses > 0.5 m thick are fully impermeable (based on the work of ref. 46).

### 21<sup>st</sup> century changes in $FAC_e$ predicted by the emulator

To discuss predicted changes in  $FAC_e$  here, we focus on the CMIP6 model-median  $FAC_e$ . The CMIP6 model-spread for each ice shelf can be found in Fig. 3 and Supplementary Table 1, and ice-shelf locations can be found in Supplementary Fig. 3. Using historical (1985–2015) ERA5 data, emulated ice-shelf  $FAC_e$  ranges from  $9.4 \pm 2.3$  m for Scar Inlet to  $25.5 \pm 0.7$  m for Venable, with a mean  $FAC_e$  for all Antarctic ice shelves ( $\overline{FAC_e}$ ) of  $16.3 \pm 2.9$  m ( $\pm 1$  standard deviation across all ice shelves; Fig. 4a). In comparison, Medley et al.<sup>23</sup> and Veldhuijsen et al.<sup>64</sup> found mean ice-shelf  $FAC_e$  values of 17.0 m between 1980 and 2021 and 15.9 m between 1979 and 2020, respectively. In East Antarctica, areas of relatively lower  $FAC_e$  occur near the ice-shelf grounding line, coinciding with observed surface meltwater ponds<sup>65</sup> (Supplementary Fig. 4). By the end of the century (2090–2100), our emulator predicts no Antarctic-wide  $\Delta \overline{FAC_e}$  under the SSP1-2.6 scenario ( $\overline{FAC_e}$  of  $16.3 \pm 3.0$  m) due to end-of-century summer air temperatures that have not increased sufficiently for substantial meltwater production and ice lens formation to occur (Supplementary Fig. 5a). For the SSP3-7.0 scenario, our emulator predicts a  $0.7 \pm 5.0$  m (4%) decrease ( $\overline{FAC_e}$  of  $15.6 \pm 4.0$  m), and for the SSP5-8.5 scenario, a  $1.3 \pm 5.4$  m (8%) decrease ( $\overline{FAC_e}$  of  $15.0 \pm 4.6$  m, Fig. 4b).

Looking at ice shelves individually, for the low-emission SSP1-2.6 scenario, very little  $\Delta FAC_e$  is predicted across most ice shelves. The only ice shelf projected to see a >10% decrease in  $FAC_e$  is Wilkins, with  $\Delta FAC_e = 2.7$  m (an 18% decrease). However, Wilkins also has the largest CMIP6 model-spread in  $\Delta FAC_e$  projections for this scenario ( $-11.0$  to  $+3.2$  m). A decline in  $FAC_e$  is more pronounced in the SSP3-7.0 scenario, where 18 of 43 ice shelves are projected to experience > a 10% decrease in  $FAC_e$ . Further, using SSP3-7.0, there are 9 ice shelves where  $FAC_e$  decreases by > 25% and 2 that decrease by > 50% (Wilkins and Scar Inlet). While a  $FAC_e$  decline is found across nearly all ice shelves in this scenario (with the exception of Ronne and Jelbart), firn air depletion is predicted to be most pronounced in the Antarctic Peninsula (AP) ( $\Delta FAC_e = -6.3$  m, a 44%

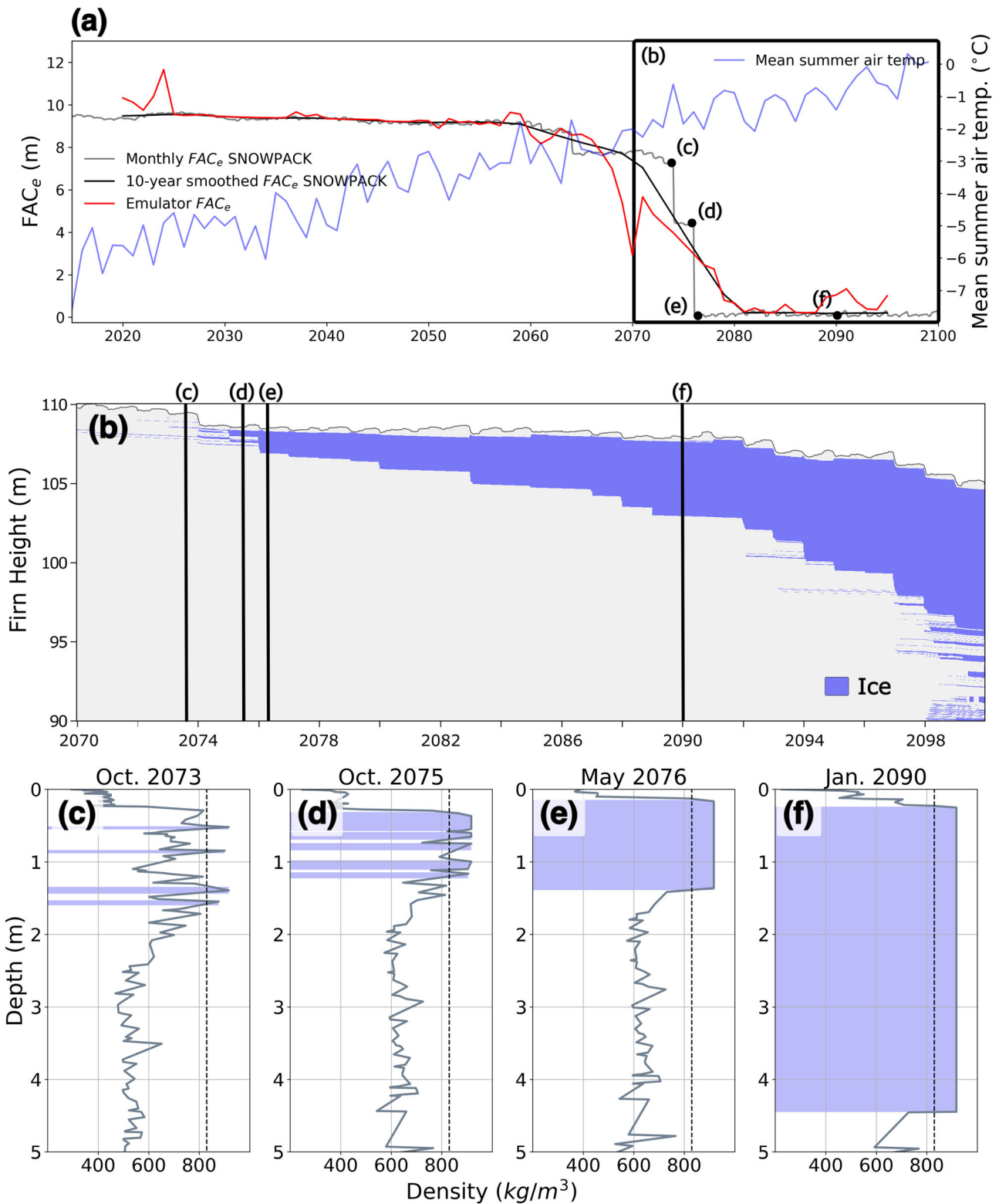


**Fig. 2 | Example SNOWPACK model result of rapid ice lens development.**  
**a** Timeseries of  $FAC_e$  from SNOWPACK forced with SSP5-8.5 CESM2 output (gray line), 10-year smoothed  $FAC_e$  from SNOWPACK (black line), emulator  $FAC_e$  (red line), and CESM2 mean summer air temperature at this site (blue line). **b** Timeseries of ice layer development (blue shading). **c-f** Vertical density profiles at different timesteps. Layers  $> 830 \text{ kg m}^{-3}$  (dashed black line) are considered to be ice lenses

(blue shading). This site is on the Southern Ross Ice Shelf (178.75 °E, 83.403141 °S, Fig. 1a yellow dot). CESM2 simulates substantially warmer historical temperatures at this site compared with ERA5 (Supplementary Fig. 2), hence warmer present day CESM2 air temperatures help promote future ice lens development under the SSP5-8.5 scenario.

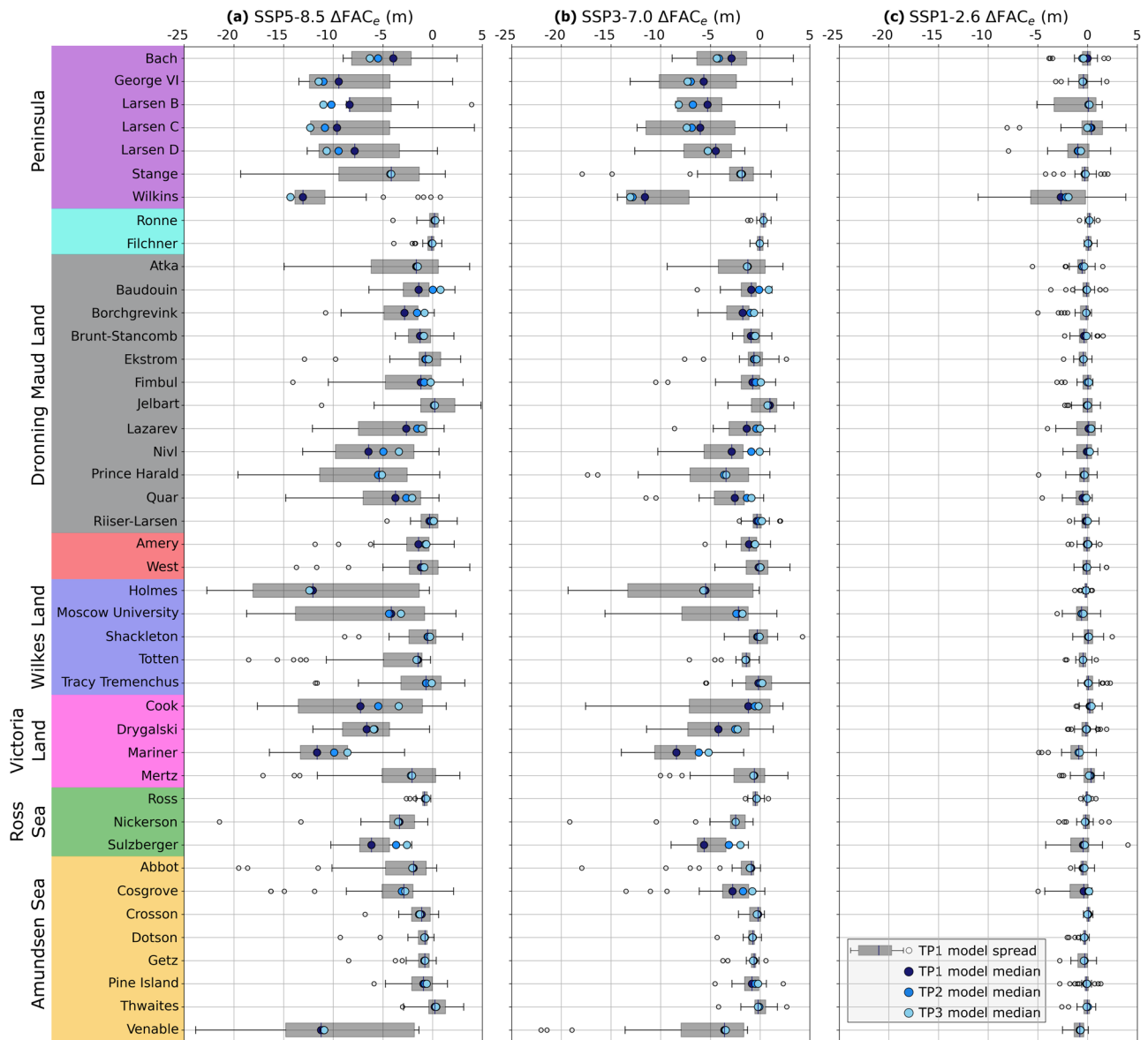


**Fig. 3 | Ice-shelf change in  $FAC_e$ .**  $\Delta FAC_e$  change from SSP5-8.5 (a), SSP3-7.0 (b) and SSP1-2.6 (c) over individual ice shelves using different ice lens thickness-permeability relationships (TP1, dark blue dot; TP2, medium blue dot; and TP3, light blue dot) and the CMIP6 model spread using TP1, Eq. (2) (Section 5.2). Box

plots show the 25<sup>th</sup> to 75<sup>th</sup> percentile spread (gray box) with whiskers representing 1.5x the interquartile range and outliers indicated by open circles. Ice shelves are grouped and shaded by region<sup>74</sup> (See Supplementary Fig. 3 for ice-shelf regions).

decrease), with Wilkins, again, projected to experience the largest  $FAC_e$  decrease (−11.6 m, or 76%).

In the high-emission SSP5-8.5 scenario, substantial firm air depletion is more widespread for ice shelves outside the AP than in lower emission scenarios. By 2100, the majority of ice shelves (22 of 43) are expected to experience a  $FAC_e$  decrease of > 10%, while 13 ice shelves experience > a 25% decrease, and 6 experience > a 50% decrease. At the end of the century, all AP ice shelves (except for Stange) have <10 m  $FAC_e$ , and Scar Inlet, Wilkins, and Larsen C have the lowest  $FAC_e$  of all Antarctic ice shelves, with 1.0, 2.1, and 3.9 m, respectively. Outside the AP, three additional ice shelves are predicted to have <10 m  $FAC_e$  by the end of the century: Mariner and Drygalski in Victoria Land with 5.7 and 6.7 m, respectively, and Nivlisen in Dronning Maud Land with 9.1 m. Additionally, Venable in the Amundsen Sea region and Holmes in Wilkes land are predicted to experience a substantial decrease in  $FAC_e$  (−11.2 and −12.1 m, respectively), although these ice shelves also have a relatively large CMIP6 model-spread in the SSP5-8.5 scenario (Fig. 3).

Antarctica’s largest ice shelves, Ronne and Ross, are projected to experience minimal  $\Delta FAC_e$  by 2100 under all emission scenarios and CMIP6 models (Figs. 3 and 4d,i). Under SSP5-8.5, Ronne has a CMIP6 model-median  $FAC_e$  increase of 0.17 m (1%) while Ross has a 0.8 m (5.2%) decrease. Coincidentally, the Amundsen Sea region in West Antarctica, where the AIS is currently losing most of its mass, is also predicted to have relatively minimal  $\Delta FAC_e$ , even in the high emission scenario. Under SSP5-8.5, ice shelves in this region are projected to lose 2.1 m  $FAC_e$ , and by 2100, Crosson, Dotson, and Getz have the highest  $FAC_e$  of all ice shelves (24.2, 23.9, and 23.2 m, respectively). Thwaites, where  $FAC_e$  increases by 0.2 m (1%), is also one of only three ice shelves in which our emulator predicts a  $FAC_e$  increase in the high emission scenario (the others being Ronne and Jelbart).

We find that 21st century ice-shelf  $\Delta FAC_e$  is mostly driven by the absolute end-of-century summer air temperature, rather than the total change in summer air temperature. In fact, the ice shelves predicted to experience the largest SSP5-8.5 CMIP6 model-mean summer air

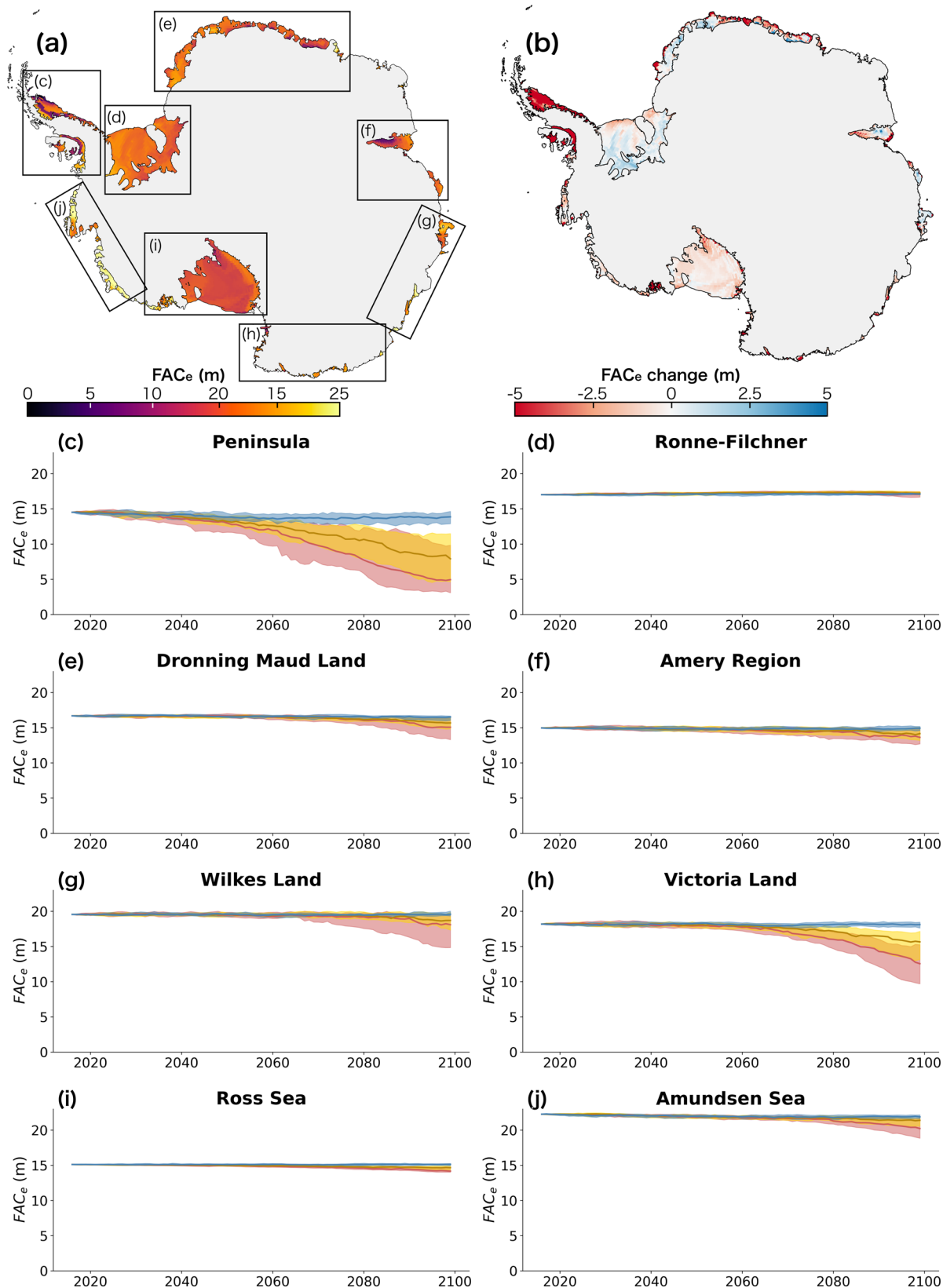


**Fig. 4 | Historical AIS ice-shelf  $FAC_e$  and 21<sup>st</sup> century  $\Delta FAC_e$ .** **a** Present-day (1985–2015)  $FAC_e$  with boxed ice-shelf regions (See Supplementary Fig. 3 for ice-shelf regions). **b** Change in  $FAC_e$  between present-day and SSP5-8.5 end-of-century (2090–2100). **c–j** Regional timeseries of 21st century  $FAC_e$  for each region shown in **(a)** and from each SSP scenario. The solid line represents the CMIP6 model-median and shading represents the 25th and 75th percentile range.

temperature increase (Filchner: +4.1 °C, Ronne: +3.9 °C, and Ross: +3.8 °C), see minimal  $FAC_e$  decrease, as described above. In contrast, Bach, Scar Inlet and Wilkins, which are predicted experience some of the largest drops in  $FAC_e$ , correspondingly have the smallest predicted summer air temperature changes (+2.4 °C for all three). Instead, these three ice shelves have some of the highest summer air temperatures expected by 2100: 0.0 °C for Bach and 0.8 °C for both Larsen B and Wilkins.

### Uncertainty in 21<sup>st</sup> century $FAC_e$

The total firn air content available for meltwater storage is impacted by the permeability of ice lenses, which inhibit vertical water movement. A major assumption we make in this work is that ice lenses impact  $FAC_e$  related to their thickness by the relationship we introduced in Eq. (1) (TP1). However, testing two alternative approaches (TP2, TP3, see Section 5.2) was found to yield similar  $\Delta FAC_e$  on both a regional and ice-sheet-wide scale. For SSP5-8.5,  $FAC_e$  across all ice shelves decreases by 1.3 m for both TP1 and TP2, and by 1.2 m using TP3. Regions that are too cold to produce consistent summer melt and thus have minimal ice lens formation, such as western Dronning Maud Land and the Ronne-Filchner and Ross regions, see minimal  $FAC_e$  decrease irrespective of the thickness-permeability relationship used (Fig. 4). We find that the thickness-permeability relationship most substantially impacts  $FAC_e$  when ice lenses are relatively thin. For example, the average AP ice-shelf  $FAC_e$  during the historical period (1985–2015) changes by approximately 1 m depending on the thickness-permeability relationship used (14.2 m from TP1, 15.8 m from TP2, and 16.6 m from TP3). By 2100, when thicker ice slabs have formed across AP ice shelves in SSP5-8.5, the thickness-permeability relationship used becomes inconsequential (4.9 m  $FAC_e$  from TP1, 5.2 m from TP2, and 5.1 m from TP3). Limited field observations of ice lens permeability make modeling this process difficult and lead to unavoidable uncertainty regarding how ice lenses impact available  $FAC_e$ .

By far the largest source of uncertainty in future  $\Delta FAC_e$  lies within CMIP6 climate model projections. For example, the 2090–2100 mean AIS-wide ice-shelf summer air temperature varies greatly across all CMIP6 models used in this study (−9.8 to −6.5 °C range in SSP1-2.6, −8.5 to −4.6 °C in SSP3-7.0, and −8.3 to −3.3 °C in SSP5-8.5). On the AP, end-of-century SSP5-8.5 CMIP6-modeled summer air temperature ranges from −2.2 to 3.7 °C, resulting in a wide range of estimated  $\Delta FAC_e$  across the different CMIP6 models (−13.0 to +1.5 m). Similarly, Wilkes Land and Victoria Land have large ranges of predicted SSP5-8.5  $\Delta FAC_e$  (−11.3 to +2.4 m for Wilkes Land and −16.5 to +0.5 m for Victoria Land). In contrast, the narrower CMIP6 model-spread of predicted  $\Delta FAC_e$  for Ronne-Filchner (−3.5 to +1.0 m) and Ross (−3.0 to +0.03 m) suggest higher confidence that these larger ice shelves will not experience drastic firn air depletion by the end of this century.

The future emission scenario used presents another source of uncertainty, the impact of which is discussed throughout Section 2.2. However, we find that CMIP6 model uncertainty, which we define as the spread in CMIP6 model projections of 21<sup>st</sup> century  $\Delta FAC_e$ , exceeds the range spanned by the emission scenarios. For example, for the AP region, where firn air depletion is expected to be the most drastic, the CMIP6-model-median  $\Delta FAC_e$  ranges from −0.65 m for SSP1-2.6 to −9.6 for SSP5-8.5, an 8.95 m spread. In comparison, the CMIP6 model range of  $\Delta FAC_e$  for SSP1-2.6, SSP3-7.0, and SSP5-8.5 is 8.9, 13.4, and 14.5 m, respectively, indicating that the CMIP6 model spread, and thus uncertainty, for SSP1-2.6 is comparable to the uncertainty across all scenarios, and for SSP3-7.0 and SSP5-8.5 is larger than the uncertainty across scenarios.

### Discussion

Our emulator was trained using output from the SNOWPACK firn model; thus, any biases present in SNOWPACK will be inherited by our emulator. Because SNOWPACK is physics-based and therefore not tuned by or biased toward observational data, it may more realistically simulate firn properties under future climate conditions that are not captured in existing observations, compared with empirical models<sup>35,66,67</sup>. SNOWPACK has been

evaluated for both Greenland and Antarctica with a consistent, identical set of model physics. In the context of this study that focuses on melt and firn hydrology, it is important to understand that SNOWPACK determines melt by solving the surface energy balance internally. SNOWPACK does not rely on externally provided melt fluxes, such as in the IMAU Firn Densification Model (IMAU-FDM)<sup>64</sup>, or calibrated factors commonly found in so-called degree-day approaches, such as currently used in the Community Firn Model (CFM)<sup>38</sup>. Degree-day models exhibit variable performance between Greenland and Antarctica<sup>23</sup> and the parameterization varies spatially<sup>68</sup>, suggesting that substantial uncertainty may arise when extrapolating degree-day approaches in future projections.

Physically-based SNOWPACK simulations have been evaluated for ice shelves<sup>39</sup>, the AIS interior<sup>35</sup>, and Greenland<sup>38</sup>, covering a wide range of climatological regimes, while relying on the same physics-based principles. For example, on Antarctic ice shelves, SNOWPACK has demonstrated a good ability to reproduce melt days and melt day variability compared with satellite microwave observations, and melt volumes compared with RACMO2.3p2 and MARv3.12<sup>39</sup>. For the Greenland Ice Sheet, SNOWPACK was found to reproduce the observed spread in  $FAC_e$  across the ice sheet over a range of climate conditions with variable amounts of melt<sup>38</sup>. Additionally, SNOWPACK accurately models the location of near-surface ice slabs compared with those detected in Operation Icebridge radar data<sup>38,59</sup>. However, firn physics are not fully understood and knowledge gaps in firn hydrological processes limit the ability of firn models to accurately simulate processes such as vertical meltwater percolation and lateral flow. As SNOWPACK is a 1-D model, it cannot simulate the relocation of meltwater via supraglacial and englacial hydrologic routing. Even though lateral meltwater flow is limited on ice shelves due to their predominantly flat topography, it may still play a role in the grounding zone regions where slopes are steeper<sup>69</sup>. More detailed observations of hydrologic firn processes are necessary to advance the development of firn models.

Inherently,  $FAC_e$  has memory of past conditions, as it is a summarizing statistic for the firn layer, which builds-up over time. However, firn has been demonstrated to have a short response time to warming conditions (less than 30 years)<sup>70</sup>. We expect that the near-surface is a relatively more important contributor to total  $FAC_e$  than deeper parts of the firn<sup>38</sup>, especially in a warming climate. As these uppermost firn layers are continuously being replenished, firn air content may more strongly reflect recent climate conditions, rather than past climate conditions. Our emulator implicitly takes past climate into account with the incorporation of the 10-year moving means. While this is sufficient for capturing large, long-term changes in  $FAC_e$ , which is the focus of this work, our emulator cannot fully capture the shorter-term interannual  $FAC_e$  variability (as seen in Fig. 2a). Supplementary Fig. 6 demonstrates that our emulator can capture long-term  $FAC_e$  changes at sites that experience none or only a partial depletion in  $FAC_e$ . Since our emulator simplifies the approximation of  $FAC_e$  by including 4 only climatological input features its utility to represent more intricate, short-term  $FAC_e$  variability is limited. Emulating this short-term variability, in addition to the large, long-term changes presented here, should be a direction for future work.

The advantage of emulation is in computational efficiency. SNOWPACK spinup takes on the order of a full day CPU time per grid point, with the final simulations taking up to a few hours CPU time per site and per scenario. In contrast, our emulator provides  $FAC_e$  estimates for 174,361 different gridcells for each of 34 different ESMs (5,928,274 total gridcells) in under 40 minutes for each emission scenario using 1 CPU core. This efficiency has enabled Antarctic-wide  $FAC_e$  investigation with multiple ESM future climates, allowing us to more fully investigate  $FAC_e$  uncertainty and spread stemming from both various ESMs and future emission scenarios. Emulation is a growing technique, providing new opportunities to create more efficient, statistical models of Earth processes. This work demonstrates the utility of emulation for studying ice sheet firn air depletion and assessing future uncertainty stemming from different ESMs and emission scenarios, and opens avenues for future research to further investigate thresholds for ice shelf instability.

Using our emulator, we find that more than 90% of all ice-shelf grid cells with mean summer air temperatures above 0 °C for any year have depleted FAC, which we define as less than 5 m FAC<sub>e</sub> (Fig. 5b). However, this summer air temperature threshold for firn air depletion appears to be lower for ice shelves that receive less precipitation (Fig. 5a), indicating that dry ice shelves may be more vulnerable to surface meltwater-induced collapse if they undergo substantial warming. This specific finding agrees with the conclusion of van Wessem et al.<sup>71</sup>. While their work was done at a higher horizontal resolution than this study, their method used a fixed threshold for melt over accumulation ratio to assess firn air depletion. This fixed threshold assumes prescribed and invariable firn properties over the ice shelves<sup>71</sup>, while our use of a physics-based, detailed firn model could be expected to better capture firn properties and melt dynamics in the firn layer in a changing climate.

While colder and dryer ice shelves may be more vulnerable to surface-melt-induced collapse at colder air temperatures than the warmer and wetter ice shelves, it is unlikely, even in the high-emission scenario, that these ice shelves will experience enough warming throughout the 21st century for substantial firn air depletion to occur. According to ERA5, the current (1985–2015) mean summer air temperature for Ronne-Filchner and Ross is −11.8 and −10.7 °C, respectively, indicating that these ice shelves would need to warm substantially to experience surface meltwater ponding. In contrast, to reach a mean summer air temperature of 0 °C, the AP Wilkins and Larsen C ice shelves need to warm only by 1.6 and 2.2 °C, respectively, a likely occurrence in most CMIP6 SSP5–8.5 and many CMIP6 SSP3–7.0 models. Areas of high, localized annual melt due to persistent warm foehn or katabatic winds (e.g. portions of the Amery or Roi Baudouin ice shelves<sup>72,73</sup>) are too small to be captured by ERA5 and the ESMs in this work. Because of this, our emulator may overestimate FAC<sub>e</sub> in these areas of high localized melt, implying that these areas may be more vulnerable to future firn air depletion than our emulator estimates.

Several factors contribute to ice-shelf vulnerability, including accumulation, surface and basal melt rates and stress regimes. Alley et al.<sup>74</sup> provides ice-shelf vulnerability indexes based on an observed relationship between annual melt days and scatterometry backscatter. In agreement with our findings, they show that AP ice shelves are the most vulnerable to surface-melt-induced firn air depletion and potential collapse, and that Ronne-Filchner and Ross are least vulnerable. However, not all ice shelves that we find are likely to experience substantial firn air depletion are susceptible to hydrofracturing and break up. For example, Lai et al.<sup>15</sup> maps ice-shelf areas where tensile stresses may promote hydrofracturing. They show that several AP ice shelves which we predict to have substantial firn air depletion such as Wilkins, Bach and George VI, have low tensile resistive stresses (including compressive stresses for George VI<sup>75</sup>), making them more resilient to hydrofracture, despite the fact that these three ice shelves usually experience widespread meltwater ponding each summer<sup>76</sup>. Additionally, ice shelves in Victoria Land, such as Mariner and Drygalski, which we project will experience substantial firn air depletion in the high-emission scenario, do not buffer substantial inland ice<sup>15</sup>, and thus would be less impactful than many other ice shelves if they were to break up. We conclude that Larsen C is the most vulnerable ice shelf to a surface-melt-induced collapse event this century due to its high likelihood of depleted FAC<sub>e</sub> and sufficiently high tensile stresses for fracture<sup>15</sup>. Further, if Larsen C does break-up, a large volume of upstream ice would be impacted because of its higher buttressing capacity compared to other ice shelves projected to experience similar firn air depletion<sup>5,15</sup>.

## Conclusions

Ice-shelf firn plays a pivotal role in preserving the stability of ice shelves, serving as a crucial reservoir for meltwater that might otherwise pond on the surface and impact ice-shelf stability. In this work, we employ the sophisticated physics-based firn model, SNOWPACK, forced with CESM2 historical and future model output over ice shelves, to capture complex thermodynamical behavior as firn transitions from dry to wet. From these firn simulations, we compute effective FAC (FAC<sub>e</sub>), an original metric that

accounts for the detrimental effect of ice lenses on subsurface meltwater percolation in the firn and FAC available for meltwater retention. We further use the FAC<sub>e</sub> derived from SNOWPACK simulations to train a statistical emulator using a random forest that replaces SNOWPACK by quickly and efficiently predicting ice-shelf FAC<sub>e</sub> based on ice-shelf climate. This approach enables us to project 21<sup>st</sup> century FAC<sub>e</sub> changes across all Antarctic ice shelves, from various future emission scenarios, and from a comprehensive suite of CMIP6 models — a task that would be computationally impractical using a traditional firn model. Our emulator indicates that mean summer air temperature is the most important climate variable for predicting firn air depletion and highlights that the Larsen C ice shelf is most critically at risk of 21<sup>st</sup> century firn air depletion.

While our analysis shows that future FAC<sub>e</sub> for some ice shelves remains relatively insensitive to climate change (e.g. Ross and Ronne-Filchner), we find a robust signal that, for this century, the fate of several Antarctic ice shelves (e.g. ice shelves in the AP or in Wilkes Land) may range from being relatively stable in low-emissions scenarios, to undergoing substantial firn air depletion in high-emission scenarios. Critically, our analysis indicates that substantial changes in FAC occur rapidly once mean summer air temperatures approach the melting point. Given the consequences of ice-shelf instability for sea-level rise projections, these findings are crucial. While many ice shelves still have large uncertainty regarding their future FAC (stemming from a wide range of CMIP6 model climate sensitivity to increased greenhouse gasses), our emulator provides a valuable tool that could be used to parameterize ice sheet models and constrain future sea-level rise projections.

## Methods

The goal of our firn emulator is to replace a more sophisticated, computationally expensive firn model to make large-scale FAC predictions into the future under a range of climatological conditions. Our firn emulator was built to mimic how the detailed, physics-based, multi-layer model SNOWPACK<sup>33,34</sup> simulates FAC under these different climatological conditions. Our methodology can be broken up into 3 main steps (Fig. 6): (a) Firn modeling using the SNOWPACK model (Section 5.1), (b) FAC<sub>e</sub> Emulator training (Section 5.2), and (c) Emulator application to predict current and future FAC<sub>e</sub> (Section 5.3).

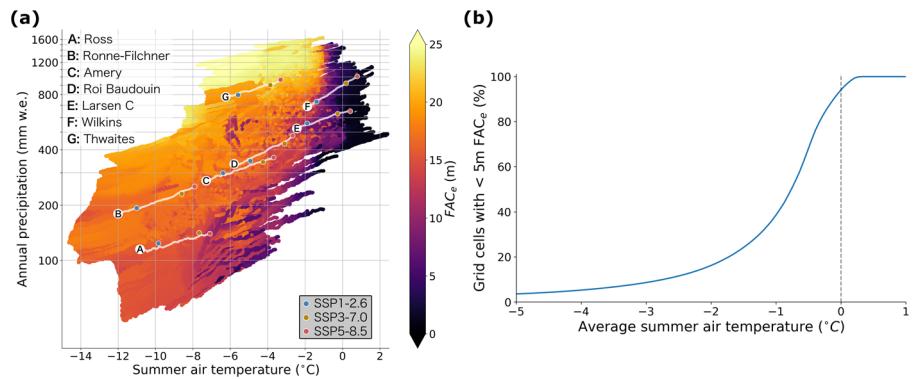
### Firn modeling using the SNOWPACK model

The SNOWPACK model has previously been modified for use on ice sheets<sup>35,36,38,77</sup> and ice shelves<sup>37,39</sup>, showing good performance at reproducing FAC over the Greenland Ice Sheet for a range of climate conditions<sup>38</sup> and good comparison of Antarctic ice shelf melt days with microwave satellite observations and melt volume with regional climate models<sup>39</sup>.

**SNOWPACK model forcing.** We forced SNOWPACK with historical and future output from National Center for Atmospheric Research's most recent Earth System Model (CESM2)<sup>40,63</sup>. Using the MEaSUREs v2 Antarctic Boundaries ice shelves map<sup>78,79</sup>, we selected 168 CESM2 ice-shelf grid cells that are representative of a variety of different ice-shelf climates (Fig. 1b). For each grid cell, we extracted 3-hourly air temperature, relative humidity and incoming shortwave radiation, and daily wind speed, incoming longwave radiation and precipitation output from CESM2 historical (1850–2015) and future (2015–2100) Shared Socio-economic Pathway (SSP) SSP1–2.6, SSP3–7.0 and SSP5–8.5 simulations<sup>80</sup>. This forcing data represents a wide range of potential climates. It is critical that firn simulations from potential future climates were included in the emulator training dataset because the historical period exhibits substantially less melt than predicted for the future and we wanted our emulator to make future FAC predictions as well.

**SNOWPACK model setup.** SNOWPACK was spun-up over the period 1850–1900 for as many repeats as necessary to build up a 100 m column of snow, firn, and ice. We then ran the final simulation from 1850–2015 for the historical scenario and 2015–2100 for each SSP scenario. Model

**Fig. 5 | FAC<sub>e</sub> and firn air depletion for different ice-shelf climate conditions.** **a** Relationship between mean summer air temperature, total annual precipitation, and FAC<sub>e</sub>. Data are from each ice-shelf grid cell below 1500 m for every year from 2015 to 2100 in the SSP3-7.0 and SSP5-8.5 scenarios. White lines represent the SSP5-8.5 projected path for seven ice shelves (A-G) with the 2090–2100 mean-state marked for SSP1-2.6 (blue dot), SSP3-7.0 (yellow dot) and SSP5-8.5 (red dot). **b** From (a), the percentage of ice-shelf grid cells with depleted firn (< 5 m FAC<sub>e</sub>) for mean summer air temperatures ranging from −5 to 1 °C.



settings were similar as described in Keenan et al.<sup>35</sup>, except for the treatment of the lower boundary for solving the heat equation for which we followed Banwell et al.<sup>39</sup> by prescribing a fixed lower-boundary temperature of −1.8 °C: the freezing point of ocean water.

**Determination of effective FAC from SNOWPACK model output.** SNOWPACK provides, among other output, the volumetric air content ( $\theta_a$ , m<sup>3</sup> m<sup>-3</sup>) in each vertical layer  $i$ . We computed effective FAC (in meters) over the  $N$  layers constituting the full firn column using:

$$FAC_e = \sum_{i=1}^N f(i)\theta_a(i)\Delta z(i) \quad (1)$$

where  $\Delta z(i)$  is the layer thickness (in meters) of layer  $i$  and  $f(i)$  is a weight applied to  $\theta_a(i)$  for each layer. The default definition of FAC is congruent with  $f(i) = 1$ , and assumes that all FAC is accessible to downward percolating meltwater. The presence of ice lenses, which we define as layers having a density > 830 kg m<sup>-3</sup> (the pore close-off density<sup>81</sup>), is known to impact how much FAC is available to retain meltwater<sup>24,41</sup>. To account for the impact that ice lenses have on meltwater storage in firn, we compute an “effective FAC” (FAC<sub>e</sub>) by varying  $f(i)$ . These  $f(i)$  weights are determined based on work by Samimi et al. (2021)<sup>46</sup>, in which the authors scale hydraulic conductivity in Darcy’s law to account for the effect of ice lenses. Based on evidence of relatively unobstructed meltwater penetration through ice layers up to 0.12 m thick at DYE-2, Greenland<sup>45</sup>, we assumed ice layers <0.1 m are fully permeable and thus all pore space below these small ice layers is included in our calculation of FAC<sub>e</sub> (i.e.,  $f(i) = 1$ ). Following Samimi et al.<sup>46</sup>, we also assumed that ice layers > 0.5 m thick are impermeable to meltwater (i.e.,  $f(i) = 0$ ), meaning that firn below these thick ice layers is excluded from our FAC<sub>e</sub> calculation. Given  $M$  ice layers above layer  $i$ , for each ice layer  $j$  above layer  $i$  with thickness  $t_j$  between 0.1 and 0.5 m, we prescribed a nonlinear decrease in FAC<sub>e</sub> below these ice layers:

$$f(i) = \sum_{j=1}^M A^{-\gamma(t_j-0.1)} \quad (2)$$

with  $A = 10$  and  $\gamma = 10^{46}$ . Weights  $f(i)$  are limited between 0 and 1. We refer to this ice lens thickness-permeability relationship as TP1 (Supplementary Fig. 7).

However, uncertainties still exist regarding how thick ice slabs can grow before they limit downward percolation of meltwater<sup>47</sup>. To test the sensitivity of our results to this assumed relationship (Eq. 2, TP1), we implement two other ice lens thickness-permeability relationships. The first alternate relationship follows Eq. (2) with  $A = 4$  and  $\gamma = 4$ , providing a less aggressive decrease in permeability with thickness (we will refer to this relationship as TP2). The other relationship we consider is also a variant of Eq. (2), applying a linear decrease in permeability with ice lens thickness

from 0.1 to 1 m (referred to as TP3):

$$f(i) = \sum_{j=1}^M 1 - \frac{t_j - 0.1}{0.9} \quad (3)$$

For both alternate relationships TP2 and TP3, we assume that ice lenses > 1 m are fully impermeable and maintain the assumption that ice lenses <0.1 m are fully permeable<sup>45,46</sup> (Supplementary Fig. 7).

### FAC<sub>e</sub> emulator training

Using FAC<sub>e</sub> derived from the SNOWPACK model output, we built an emulator which allows us to efficiently estimate FAC<sub>e</sub> across all Antarctic ice shelves for numerous climate model scenarios. Our emulator was built using a random forest (RF) model<sup>82</sup>, which we trained and implemented using the Python sci-kit learn library<sup>83</sup>. We opted for a RF as it has demonstrated good performance in emulating model processes<sup>50</sup>, even compared with deep neural networks and gaussian processes<sup>51</sup>, can learn nonlinear behavior, and is quick to train and implement. Additionally, RFs provide out-of-bag estimates, a useful validation metric, and feature importance measures, allowing use to assess which climate conditions are most important for FAC<sub>e</sub> predictions<sup>52</sup>. Briefly, RFs consist of an ensemble of decision trees. The RF inputs are referred to as ‘features’ and a prediction for the output, or ‘target’, variable is made by averaging this ensemble.

**FAC<sub>e</sub> emulator feature and target variables.** To train our emulator, we used historical (1985–2015) and future (2015–2100) SSP1-2.6, SSP3-7.0, and SSP5-8.5 climate variable output from CESM2 at each grid cell where we ran SNOWPACK. The climate variables used as features in our emulator (to predict FAC<sub>e</sub>) were: (1) total annual precipitation, (2) mean annual 10 m wind speed, (3) mean annual 2 m air temperature and (4) mean austral summer (DJF) 2 m air temperature. These variables are 1) known to impact surface firn density, compaction rate and meltwater production, all which impact FAC<sub>e</sub>, and 2) readily available from most Earth System Models. We only consider total precipitation and not precipitation type because 1) precipitation partitioned into solid and liquid precipitation is less common GCM output, and 2) our emulator was shown to have a low FAC<sub>e</sub> bias at sites with higher summer air temperatures (Fig. 1c), indicating that neglecting to account for temporal changes in the rain/snow ratio has not led to a substantial source of error.

Our target variable was October mean FAC<sub>e</sub> (just before the melt season onset) at corresponding timesteps and locations.

**Feature and target variable preprocessing.** We computed 10-year moving averages of our feature and target variables to largely remove interannual variability and achieve a more representative mean climate, at the expense of capturing inter-annual variability. As a result, our input dataset consisted of 21-timesteps of 10-year moving means from the historical period (1990–2010) and 76-timesteps of 10-year moving

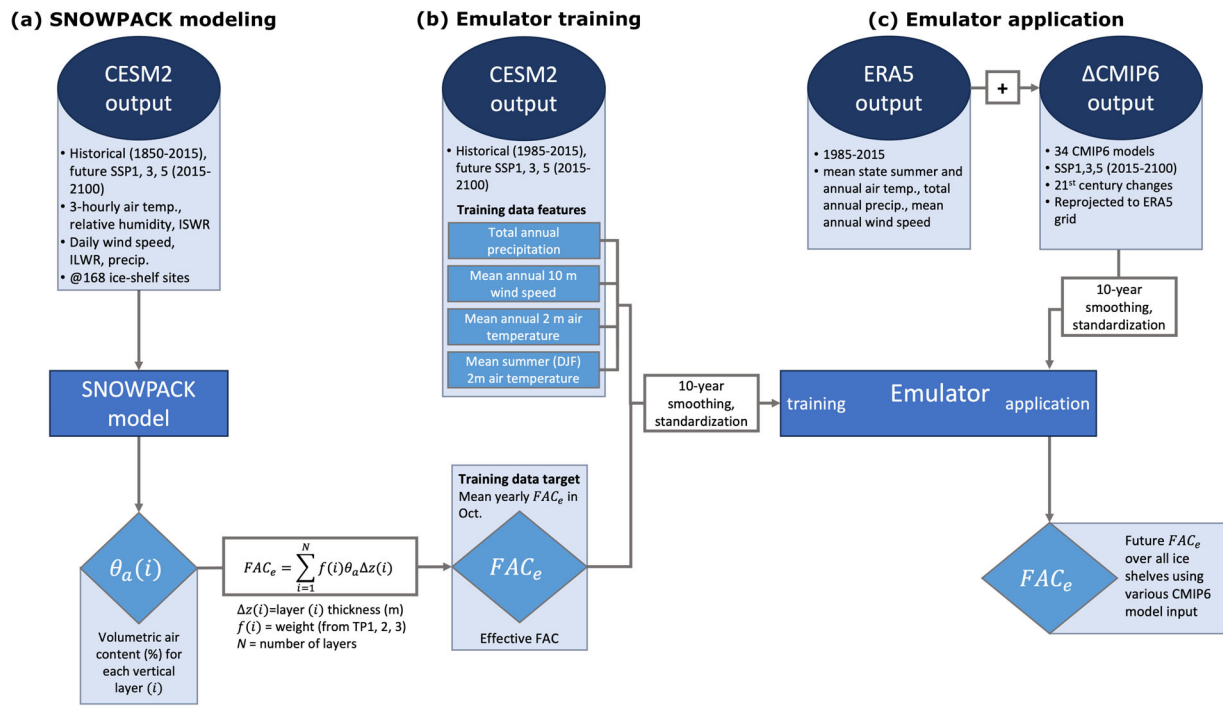


**Fig. 6 | Schematic outlining our methodology.** Steps (a), (b), and (c) follow Section 5.1 Firm modeling using the SNOWPACK model, 5.2  $FAC_e$  Emulator training, and 5.3  $FAC_e$  Emulator application, respectively.

means from future emission scenarios SSP1-2.6, SSP3-7.0 and SSP5-8.5 (2020–2095) at each of the 168 ice-shelf sites for which we employed SNOWPACK. In total, our input dataset consisted of 41,832 entries (168 sites \* (21 historical years + 76 future years \* 3 scenarios)), which we divided into two groups such that 80% was used for model training and 20% was used for testing. Additionally, we held out 4 ice-shelves (Venable, Brunt Stancomb, Totten, and Larsen C) completely from the training dataset, to test our emulator with previously unseen ice-shelves. Supplementary Fig. 8 demonstrates that the variability in ice-shelf climate regimes is sufficiently captured by the training dataset and that our emulator can reproduce 21<sup>st</sup> century firm air depletion on previously unseen ice shelves.

To maximize the points used for training, the emulator does not consider dependence in  $FAC_e$  between successive years. This dependence, however, is implicitly captured through the 10-year moving averaged inputs. No additional filtering was done besides the 10-year moving means. Finally, we standardize our training data feature and target variables by subtracting the mean and dividing by the standard deviation for each variable.

**Emulator hyperparameter tuning.** Our RF was comprised of 100 decision trees, each optimized on a bootstrapped sample of the training dataset. The hyperparameters used for our RF model are listed below (*points in italics* indicate parameters that differ from the scikit-learn default):

- Number of trees (`'n_estimators'`) = 100
- Costfunction (`'criterion'`) = L2 loss (`'squared_error'`)
- Maximum tree depth (`'max_depth'`) = None
- Minimum samples required to split a node (`'min_samples_split'`) = 2
- Minimum leaf size = `'min_samples_leaf'` = 1
- Number of features to consider when looking for the best split (`'max_features'`) = `'auto'`
- `'bootstrap'` = True
- Use *out-of-bag* samples to estimate the generalization score (`'oob_score'`) = True

- Number of samples to draw from X to train each base estimator (`'max_samples'`) = None

To test our RF hyperparameter choice we randomly selected 100 different combinations of the following scikit-learn hyperparameters:

- `'max_depth'` = [5, 10, 25, 50, 100, None]
- `'max_features'` = [`'auto'`, `'sqrt'`]
- `'min_samples_leaf'` = [1, 2, 4]
- `'min_samples_split'` = [2, 5, 10]
- `'n_estimators'` = [10, 50, 100, 200]

The optimal hyperparameters from this randomized search were: `'max_depth'` = None, `'max_features'` = `'sqrt'`, `'min_samples_leaf'` = 1, `'min_samples_split'` = 2, `'n_estimators'` = 200. We then compared this optimal model from our randomized search with the default hyperparameters and found that the default model had a marginally better mean 5-fold cross validation score (0.9526 ± 0.0033 for the default model and 0.9522 ± 0.0031). As such, we chose to use the default scikit-learn hyperparameters for our random forest, except for `'oob_score'` = True, which we used as a validation metric for the model's generalization error.

**Emulator application to predict current and future  $FAC_e$**

**Current  $FAC_e$ .** We estimated present-day (1985-2015) ice-shelf  $FAC_e$  by running our firm emulator with input data from the ECMWF ERA5 reanalysis dataset<sup>53</sup>. We used ERA5 because it has the smallest near-surface temperature bias relative to the observations and best represents accumulation<sup>84,85</sup>. We only considered ice shelves with > 5 ERA5 grid cells with a modeled elevation <1500 m above sea level, resulting in 43 ice shelves, which we divided into 8 regions<sup>74</sup> for a regional comparison of FAC (Supplementary Fig. 3).

**Future  $FAC_e$ .** To predict ice-shelf  $FAC_e$  throughout the 21st century, we used changes in mean annual near-surface air temperature,

summer air temperature, wind speed, and total annual precipitation from CMIP6 models<sup>54</sup> (Supplementary Table 2). From the 88 available CMIP6 models, we only used the 34 models with these variables available on the Pangeo platform from the historical period and future SSP1-2.6, SSP3-7.0, and SSP5-8.5 scenarios. To map a future FAC<sub>e</sub> envelope, we used the low-emission (SSP1-2.6) and high-emission (SSP5-8.5) scenarios, and included SSP3-7.0 as a more likely high-end emission scenario<sup>86</sup>. CMIP6 model output was regridded using bilinear interpolation to the ERA5 grid. Changes in these climate variables were added to the ‘current-state’ climate from ERA5 to remove possible bias in the CMIP6 models representation of the current climate (delta-change method<sup>87,88</sup>). We again computed 10-year moving averages (from 2020–2095) of these climate variables as input for the emulator.

To determine the 21st century  $\Delta$ FAC<sub>e</sub>, we subtract the mean historical (1985–2015) FAC<sub>e</sub> from the 2095 value, which represents an end-of-century mean-state FAC<sub>e</sub>, because our emulator input is 10-year moving averages of climate variables. We calculate % change in FAC<sub>e</sub> with respect to the total ice-shelf FAC<sub>e</sub>, not for each grid cell.

Additionally, we ensured that the dataset used for training our emulator covers the range of climatic conditions used in its application with CMIP6 models. We compared climate conditions used for training (raw-CESM2 output) with conditions used in the emulator simulations (ERA5 +  $\Delta$ ESM mean). Supplementary Fig. 5b shows that the emulator simulations do not extrapolate greatly beyond the data used for training. In cases where extrapolation does occur (e.g. the Ronne ice shelf where ERA5 historical conditions are colder than the training dataset), FAC<sub>e</sub> change will be minimal and the emulator performs as expected given these colder conditions. Further, the firn air depletion transition is well represented in the training data and thus the training data set is appropriate for how we implement the emulator.

### Code availability

The SNOWPACK model code is available at: <https://github.com/snowpack-model/snowpack>. Code used for the analysis in the project is published at <https://doi.org/10.5281/zenodo.10456145>.

### Data availability

ERA5 reanalysis output can be downloaded at <https://doi.org/10.24381/cds.adbb2d47>. Input and FAC results from the SNOWPACK model can be found at <https://doi.org/10.5281/zenodo.7535507>. The emulator models and emulator FAC results can be found at <https://doi.org/10.5281/zenodo.10456145>. Instructions and examples for how to access CMIP6 model output from the Pangeo Platform can be found at <https://gallery.pangeo.io/repos/pangeo-gallery/cmip6/>.

Received: 6 July 2023; Accepted: 2 February 2024;

Published online: 24 February 2024

### References

- Otosaka, I. N. et al. Mass balance of the Greenland and Antarctic ice sheets from 1992 to 2020. *Earth Syst. Sci. Data* **15**, 1597–1616 (2023).
- Bell, R. E. & Seroussi, H. History, mass loss, structure, and dynamic behavior of the Antarctic Ice Sheet. *Science (1979)* **367**, 1321–1325 (2020).
- Pattyn, F. et al. The Greenland and Antarctic ice sheets under 1.5 °C global warming. *Nat. Clim. Chang.* **8**, 1053–1061 (2018).
- Dupont, T. K. & Alley, R. B. Assessment of the importance of ice-shelf buttressing to ice-sheet flow. *Geophys. Res. Lett.* **32**, 1–4 (2005).
- Fürst, J. J. et al. The safety band of Antarctic ice shelves. *Nat. Clim. Chang.* **6**, 479–482 (2016).
- Rignot, E. et al. Accelerated ice discharge from the Antarctic Peninsula following the collapse of Larsen B ice shelf. *Geophys. Res. Lett.* **31**, 2–5 (2004).
- De Angelis, H. & Skvarca, P. Glacier surge after ice shelf collapse. *Science (1979)* **299**, 1560–1562 (2003).
- Greene, C. A., Gardner, A. S., Schlegel, N.-J. & Fraser, A. D. Antarctic calving loss rivals ice-shelf thinning. *Nature* **609**, 948–953 (2022).
- Pritchard, H. D. et al. Antarctic ice-sheet loss driven by basal melting of ice shelves. *Nature* **484**, 502–505 (2012).
- Depoorter, M. A. et al. Calving fluxes and basal melt rates of Antarctic ice shelves. *Nature* **502**, 89–92 (2013).
- Liu, Y. et al. Ocean-driven thinning enhances iceberg calving and retreat of Antarctic ice shelves. *Proc. Natl. Acad. Sci. USA* (2015) <https://doi.org/10.1073/pnas.1415137112>.
- van den Broeke, M. Strong surface melting preceded collapse of Antarctic Peninsula ice shelf. *Geophys. Res. Lett.* **32**, L12815 (2005).
- Scambos, T. A., Hulbe, C., Fahnestock, M. & Bohlander, J. The link between climate warming and break-up of ice shelves in the Antarctic Peninsula. *J. Glaciol.* **46**, 516–530 (2000).
- Holland, P. R. et al. Oceanic and atmospheric forcing of Larsen C Ice-Shelf thinning. *Cryosphere* **9**, 1005–1024 (2015).
- Lai, C. Y. et al. Vulnerability of Antarctica’s ice shelves to meltwater-driven fracture. *Nature* **584**, 574–578 (2020).
- van der Veen, C. J. Fracture propagation as means of rapidly transferring surface meltwater to the base of glaciers. *Geophys. Res. Lett.* **34**, L01501 (2007).
- Banwell, A. F., MacAyeal, D. R. & Sergienko, O. V. Breakup of the Larsen B Ice Shelf triggered by chain reaction drainage of supraglacial lakes. *Geophys. Res. Lett.* **40**, 5872–5876 (2013).
- Robel, A. A. & Banwell, A. F. A speed limit on ice shelf collapse through hydrofracture. *Geophys. Res. Lett.* **46**, 12092–12100 (2019).
- Leeson, A. A., Forster, E., Rice, A., Gourmelen, N. & van Wessem, J. M. Evolution of supraglacial lakes on the Larsen B ice shelf in the decades before it collapsed. *Geophys. Res. Lett.* **47**, e2019GL085591 (2020).
- Scambos, T. A. et al. Ice shelf disintegration by plate bending and hydro-fracture: Satellite observations and model results of the 2008 Wilkins ice shelf break-ups. *Earth Planet. Sci. Lett.* **280**, 51–60 (2009).
- Pattyn, F. & Morlighem, M. The uncertain future of the Antarctic Ice Sheet. *Science (1979)* **367**, 1331–1335 (2020).
- van Wessem, J. M. et al. Modelling the climate and surface mass balance of polar ice sheets using RACMO2 – Part 2: Antarctica (1979–2016). *Cryosphere* **12**, 1479–1498 (2018).
- Medley, B., Neumann, T. A., Zwally, H. J., Smith, B. E. & Stevens, C. M. Simulations of firn processes over the Greenland and Antarctic ice sheets: 1980–2021. *Cryosphere* **16**, 3971–4011 (2022).
- Munneke, P. K., Ligtenberg, S. R. M., Van Den Broeke, M. R. & Vaughan, D. G. Firn air depletion as a precursor of Antarctic ice-shelf collapse. *J. Glaciol.* **60**, 205–214 (2014).
- Massom, R. A. et al. Antarctic ice shelf disintegration triggered by sea ice loss and ocean swell. *Nature* **558**, 383–389 (2018).
- MacAyeal, D. R., Scambos, T. A., Hulbe, C. L. & Fahnestock, M. A. Catastrophic ice-shelf break-up by an ice-shelf-fragment-capsize mechanism. *J. Glaciol.* **49**, 22–36 (2003).
- Braun, M. & Humbert, A. Recent retreat of Wilkins ice shelf reveals new insights in ice shelf breakup mechanisms. *IEEE Geosci. Remote Sensing Lett.* **6**, 263–267 (2009).
- Laffin, M. K., Zender, C. S., van Wessem, M. & Marinsek, S. The role of föhn winds in eastern Antarctic Peninsula rapid ice shelf collapse. *Cryosphere* **16**, 1369–1381 (2022).
- Wille, J. D. et al. The extraordinary March 2022 East Antarctica “heat” wave. Part II: impacts on the Antarctic ice sheet. *J. Clim.* (2023) <https://doi.org/10.1175/JCLI-D-23-0176.1>.
- Gilbert, E. & Kittel, C. Surface Melt and Runoff on Antarctic Ice Shelves at 1.5 °C, 2 °C, and 4 °C of Future Warming. *Geophys. Res. Lett.* **48**, e2020GL091733 (2021).
- van den Broeke, M. R. et al. Contrasting current and future surface melt rates on the ice sheets of Greenland and Antarctica: Lessons

- from in situ observations and climate models. *PLOS Clim.* **2**, e0000203 (2023).
32. Donat-Magnin, M. et al. Future surface mass balance and surface melt in the Amundsen sector of the West Antarctic Ice Sheet. *Cryosphere* **15**, 571–593 (2021).
  33. Bartelt, P. & Lehning, M. A physical SNOWPACK model for the Swiss avalanche warning Part I: Numerical model. *Cold Reg. Sci. Technol.* **35**, 123–145 (2002).
  34. Lehning, M., Bartelt, P., Brown, B., Fierz, C. & Satyawali, P. A physical SNOWPACK model for the Swiss avalanche warning Part II. Snow microstructure. *Cold Reg. Sci. Technol.* **35**, 147–167 (2002).
  35. Keenan, E. et al. Physics-based SNOWPACK model improves representation of near-surface Antarctic snow and firn density. *Cryosphere* **15**, 1065–1085 (2021).
  36. Dunmire, D. et al. Observations of buried lake drainage on the Antarctic Ice Sheet. *Geophys. Res. Lett.* **47**, e2020GL087970 (2020).
  37. Alley, K. E. et al. Two decades of dynamic change and progressive destabilization on the Thwaites Eastern Ice Shelf. *Cryosphere* **15**, 5187–5203 (2021).
  38. Thompson-Munson, M., Wever, N., Stevens, C. M., Lenaerts, J. T. M. & Medley, B. An evaluation of a physics-based firn model and a semi-empirical firn model across the Greenland Ice Sheet (1980–2020). *Cryosphere* **17**, 2185–2209 (2023).
  39. Banwell, A. F., Wever, N., Dunmire, D. & Picard, G. Quantifying Antarctic-Wide Ice-Shelf Surface Melt Volume Using Microwave and Firn Model Data: 1980 to 2021. *Geophys. Res. Lett.* **50**, (2023). <https://doi.org/10.1029/2023GL102744>.
  40. Danabasoglu, G. et al. The Community Earth System Model Version 2 (CESM2). *J. Adv. Model Earth Syst.* **12**, 1–35 (2020).
  41. Machguth, H. et al. Greenland meltwater storage in firn limited by near-surface ice formation. *Nat. Clim. Chang.* **6**, 390–393 (2016).
  42. Vandecrux, B. et al. The firn meltwater Retention Model Intercomparison Project (RetMIP): evaluation of nine firn models at four weather station sites on the Greenland ice sheet. *Cryosphere* **14**, 3785–3810 (2020).
  43. Brils, M., Kuipers Munneke, P., van de Berg, W. J. & van den Broeke, M. Improved representation of the contemporary Greenland ice sheet firn layer by IMAU-FDM v1.2G. *Geosci. Model Dev.* **15**, 7121–7138 (2022).
  44. Steger, C. R. et al. Firn Meltwater Retention on the Greenland Ice Sheet: A Model Comparison. *Front. Earth Sci.* **5**, (2017). <https://doi.org/10.3389/feart.2017.00003>
  45. Samimi, S., Marshall, S. J. & MacFerrin, M. Meltwater penetration through temperate ice layers in the percolation zone at DYE-2, greenland ice sheet. *Geophys. Res. Lett.* **47**, 1–9 (2020).
  46. Samimi, S., Marshall, S. J., Vandecrux, B. & MacFerrin, M. Time-Domain Reflectometry Measurements and Modeling of Firn Meltwater Infiltration at DYE-2, Greenland. *J. Geophys. Res. Earth Surf.* **126**, (2021). <https://doi.org/10.1029/2021JF006295>.
  47. Ashmore, D. W., Mair, D. W. F. & Burgess, D. O. Meltwater percolation, impermeable layer formation and runoff buffering on Devon Ice Cap, Canada. *J. Glaciol.* **66**, 61–73 (2020).
  48. O'Hagan, A. Bayesian analysis of computer code outputs: A tutorial. *Reliab. Eng. Syst. Saf.* **91**, 1290–1300 (2006).
  49. Verjans, V. et al. Uncertainty in east antarctic firn thickness constrained using a model ensemble approach. *Geophys. Res. Lett.* **48**, 1–11 (2021).
  50. O'Gorman, P. A. & Dwyer, J. G. Using machine learning to parameterize moist convection: potential for modeling of climate, climate change, and extreme events. *J. Adv. Model Earth Syst.* **10**, 2548–2563 (2018).
  51. Lim, T. & Wang, K. Comparison of machine learning algorithms for emulation of a gridded hydrological model given spatially explicit inputs. *Comput. Geosci.* **159**, 105025 (2022).
  52. Archer, K. J. & Kimes, R. V. Empirical characterization of random forest variable importance measures. *Comput. Stat. Data Anal.* **52**, 2249–2260 (2008).
  53. Hersbach, H. et al. The ERA5 global reanalysis. *Quarterly J. R. Meteorolog. Soc.* **146**, 1999–2049 (2020).
  54. Eyring, V. et al. Overview of the Coupled Model Intercomparison Project Phase 6 (CMIP6) experimental design and organization. *Geosci. Model Dev.* **9**, 1937–1958 (2016).
  55. Veldhuijsen, S. B. M., van de Berg, W. J., Munneke, P. K. & van den Broeke, M. R. Evolution of Antarctic firn air content under three future warming scenarios. *The Cryosphere Discussions* [preprint] (2023). <https://doi.org/10.5194/egusphere-2023-2237>.
  56. Gettelman, A. et al. High Climate Sensitivity in the Community Earth System Model Version 2 (CESM2). *Geophys. Res. Lett.* **46**, 8329–8337 (2019).
  57. Nembrini, S., König, I. R. & Wright, M. N. The revival of the Gini importance? *Bioinformatics* **34**, 3711–3718 (2018).
  58. Trusel, L. D. et al. Divergent trajectories of Antarctic surface melt under two twenty-first-century climate scenarios. *Nat. Geosci.* **8**, 927–932 (2015).
  59. MacFerrin, M. et al. Rapid expansion of Greenland's low-permeability ice slabs. *Nature* **573**, 403–407 (2019).
  60. Jullien, N., Tedstone, A. J., Machguth, H., Karlsson, N. B. & Helm, V. Greenland Ice Sheet Ice Slab Expansion and Thickening. *Geophys. Res. Lett.* **50**, (2023). <https://doi.org/10.1029/2022GL100911>.
  61. Culberg, R., Schroeder, D. M. & Chu, W. Extreme melt season ice layers reduce firn permeability across Greenland. *Nat. Commun.* **12**, 2336 (2021).
  62. Rennermalm, Å. K. et al. Shallow firn cores 1989–2019 in southwest Greenland's percolation zone reveal decreasing density and ice layer thickness after 2012. *J. Glaciol.* **68**, 431–442 (2022).
  63. Dunmire, D., Lenaerts, J. T. M., Datta, R. T. & Gorte, T. Antarctic surface climate and surface mass balance in the Community Earth System Model version 2 during the satellite era and into the future (1979–2100). *Cryosphere* **16**, 4163–4184 (2022).
  64. Veldhuijsen, S. B. M., van de Berg, W. J., Brils, M., Kuipers Munneke, P. & van den Broeke, M. R. Characteristics of the 1979–2020 Antarctic firn layer simulated with IMAU-FDM v1.2A. *Cryosphere* **17**, 1675–1696 (2023).
  65. Stokes, C. R., Sanderson, J. E., Miles, B. W. J., Jamieson, S. S. R. & Leeson, A. A. Widespread distribution of supraglacial lakes around the margin of the East Antarctic Ice Sheet. *Sci. Rep.* **9**, 1–14 (2019).
  66. van Kampenhout, L. et al. Improving the representation of polar snow and firn in the community earth system model. *J. Adv. Model Earth Syst.* **9**, 2583–2600 (2017).
  67. Lundin, J. M. D. et al. Firn Model Intercomparison Experiment (FirnMICE). *J. Glaciol.* **63**, 401–422 (2017).
  68. Zheng, Y., Gолledge, N. R., Gossart, A., Picard, G. & Leduc-Leballeur, M. Statistically parameterizing and evaluating a positive degree-day model to estimate surface melt in Antarctica from 1979 to 2022. *Cryosphere* **17**, 3667–3694 (2023).
  69. Dell, R. et al. Lateral meltwater transfer across an Antarctic ice shelf. *Cryosphere* **14**, 2313–2330 (2020).
  70. Munneke, P. K., Ligtenberg, S. R. M., Suder, E. A. & Van den Broeke, M. R. A model study of the response of dry and wet firn to climate change. *Ann. Glaciol.* **56**, 1–8 (2015).
  71. van Wessem, J. M., van den Broeke, M. R., Wouters, B. & Lhermitte, S. Variable temperature thresholds of melt pond formation on Antarctic ice shelves. *Nat. Clim. Chang.* **13**, 161–166 (2023).
  72. Zwally, H. J. & Fiegles, S. Extent and duration of Antarctic surface melting. *J. Glaciol.* **40**, 463–476 (1994).
  73. Lenaerts, J. T. M. et al. Meltwater produced by wind-albedo interaction stored in an East Antarctic ice shelf. *Nat. Clim. Chang.* **7**, 58–62 (2017).

74. Alley, K. E., Scambos, T. A., Miller, J. Z., Long, D. G. & MacFerrin, M. Quantifying vulnerability of Antarctic ice shelves to hydrofracture using microwave scattering properties. *Remote Sens. Environ.* **210**, 297–306 (2018).
75. Labarbera, C. H. & Macayeal, D. R. Traveling supraglacial lakes on George VI Ice Shelf. *Antarctica* **38**, 1–5 (2011).
76. Banwell, A. F. et al. The 32-year record-high surface melt in 2019/2020 on the northern George VI Ice Shelf, Antarctic Peninsula. *Cryosphere* **15**, 909–925 (2021).
77. Dunmire, D., Banwell, A., Lenaerts, J. & Datta, R. T. Contrasting regional variability of buried meltwater extent over two years across the Greenland Ice Sheet. *Cryosphere* **15**, 2983–3005 (2021).
78. Mougnot, J., Scheuchl, B. & Rignot, E. MEaSURES Antarctic Boundaries for IPY 2007–2009 from Satellite Radar, Version 2. <https://doi.org/10.5067/AXE4121732AD> (2017).
79. Rignot, E., Mougnot, J. & Scheuchl, B. MEaSURES Antarctic Grounding Line from Differential Satellite Radar Interferometry, Version 2. *NASA National Snow and Ice Data Center Distributed Active Archive Center* (2016) <https://doi.org/10.5067/IKBWW4RYHF1Q>.
80. Meinshausen, M. et al. The shared socio-economic pathway (SSP) greenhouse gas concentrations and their extensions to 2500. *Geosci. Model Dev.* **13**, 3571–3605 (2020).
81. Martinerie, P., Raynaud, D., Etheridge, D. M., Barnola, J.-M. & Mazaudier, D. Physical and climatic parameters which influence the air content in polar ice. *Earth Planet Sci. Lett.* **112**, 1–13 (1992).
82. Breiman, L. Random forests. *Mach. Learn.* **45**, 5–32 (2001).
83. Pedregosa, F. et al. Scikit-learn: Machine Learning in Python. *J. Mach. Learning Res.* **12**, 2825–2830 (2011).
84. Gossart, A. et al. An evaluation of surface climatology in state-of-the-art reanalyses over the Antarctic Ice Sheet. *J. Clim.* **32**, 6899–6915 (2019).
85. Zhu, J. et al. An Assessment of ERA5 Reanalysis for Antarctic Near-Surface Air Temperature. *Atmosphere (Basel)* **12**, e8062 (2021).
86. IPCC. *IPCC, 2021: Climate Change 2021: The Physical Science Basis. Contribution of Working Group I to the Sixth Assessment Report of the Intergovernmental Panel on Climate Change.* (2021).
87. Rummukainen, M. State-of-the-art with regional climate models. *Clim. Change* **1**, 82–96 (2010).
88. Maraun, D. Bias correcting climate change simulations - a critical review. *Curr. Clim. Change Rep.* **2**, 211–220 (2016).

## Acknowledgements

D.D. was supported by NASA FINESST Fellowship #80NSSC19K1329 and by the iHARP HDR Institute (NSF award #2118285). A.F.B. received support from the NSF under award #1841607 to the University of Colorado Boulder. N.W. was supported by NASA IDS grant #80NSSC20K1727 and the Swiss National Science Foundation (SNSF Grant 200020-179130). We acknowledge high-performance computing support from Cheyenne (<https://doi.org/10.5065/D6RX99HX>) provided by NCAR's Computational and Information Systems Laboratory, sponsored by the NSF. This work also

utilized the Summit supercomputer, which is supported by the NSF (awards ACI-1532235 and ACI-1532236) and is a joint effort of the University of Colorado Boulder, and Colorado State University. Data storage supported by the University of Colorado Boulder 'PetaLibrary'. We would additionally like to acknowledge the editor, Aliénor Lavergne, and three anonymous reviewers for their thoughtful and helpful comments that greatly improved the manuscript.

## Author contributions

DD and JLM initially designed the study. DD led the analysis and writing. NW contributed to the SNOWPACK model setup, analysis, and interpretation. AFB helped interpret the results of the emulator. All authors contributed to study design, interpretation, and writing.

## Competing interests

The authors declare no competing interests.

## Additional information

**Supplementary information** The online version contains supplementary material available at <https://doi.org/10.1038/s43247-024-01255-4>.

**Correspondence** and requests for materials should be addressed to Devon Dunmire.

**Peer review information** *Communications Earth & Environment* thanks the anonymous reviewers for their contribution to the peer review of this work. Primary Handling Editor: Aliénor Lavergne. A peer review file is available.

**Reprints and permissions information** is available at <http://www.nature.com/reprints>

**Publisher's note** Springer Nature remains neutral with regard to jurisdictional claims in published maps and institutional affiliations.

**Open Access** This article is licensed under a Creative Commons Attribution 4.0 International License, which permits use, sharing, adaptation, distribution and reproduction in any medium or format, as long as you give appropriate credit to the original author(s) and the source, provide a link to the Creative Commons licence, and indicate if changes were made. The images or other third party material in this article are included in the article's Creative Commons licence, unless indicated otherwise in a credit line to the material. If material is not included in the article's Creative Commons licence and your intended use is not permitted by statutory regulation or exceeds the permitted use, you will need to obtain permission directly from the copyright holder. To view a copy of this licence, visit <http://creativecommons.org/licenses/by/4.0/>.

© The Author(s) 2024